AIAA 99-3260

Comparison of Several Spatial Discretizations for the Navier-Stokes Equations

D. W. Zingg, S. De Rango, M. Nemec,
Institute for Aerospace Studies
University of Toronto
Toronto, Ontario, Canada

and

T. H. Pulliam
NASA Ames Research Center
Moffett Field, CA 94035, USA

14th AIAA Computational Fluid Dynamics Conference

June 28-July 1, 1999/Norfolk, VA

Comparison of Several Spatial Discretizations for the Navier-Stokes Equations

D. W. Zingg,* S. De Rango,† M. Nemec,‡
Institute for Aerospace Studies
University of Toronto
Toronto, Ontario, Canada

and

T. H. Pulliam§
NASA Ames Research Center
Moffett Field, CA 94035, USA

Grid convergence studies for subsonic and transonic flows over airfoils are presented in order to compare the accuracy of several spatial discretizations for the compressible Navier-Stokes equations. The spatial discretizations include the following treatment of the inviscid fluxes: 1) second-order centered differences with third-order matrix artificial dissipation, 2) the second-order convective upstream split pressure scheme (CUSP), 3) third-order upwind-biased differencing with Roe's flux-difference splitting, and 4) fourth-order centered differences with third-order matrix artificial dissipation. The first three schemes are combined with second-order differencing for the viscous terms. The fourth scheme uses fourth-order differencing for the viscous terms, as well as higher-order approximations near boundaries and for the numerical integration. The grid convergence studies indicate that for subsonic flows, the scheme using higher-order differencing for both viscous and inviscid fluxes is substantially more accurate than the others, producing less than one percent numerical error in drag even on coarse grids. For transonic flows, this scheme is again the most accurate, but somewhat finer grids are required to achieve less than one percent error in drag. The formulation of the limiter function is shown to be an important consideration in computing transonic flows.

Introduction

MANY different algorithms have been developed for the numerical solution of the steady compressible Navier-Stokes equations. It is essential that such algorithms be both reliable and efficient, where efficiency is measured in terms of the computational effort required to achieve a given level of accuracy. Most algorithms in use for steady flows can be divided into two distinct components, a discretization of the spatial derivatives in the governing partial differential equations and an iterative method for driving the discretized equations to a steady state. For this class of algorithms, the accuracy of a converged steady solution depends only on the spatial discretization and is independent of the iterative method. The nature of the spatial discretization affects the efficiency of the overall algorithm through 1) its computational cost per node per iteration, 2) its accuracy, i.e., its effect on the number of grid nodes required to achieve a given level of numerical accuracy (independent of physical model error), and 3) its effect on the convergence rate of the iterative method and thus the total number of iterations needed to reach a steady state.

The discretization of the inviscid flux terms has received considerable attention. It often consists of the following components:

1. A discrete approximation of the flux derivatives applicable to scalar flux functions, typically valid to some order of accuracy, including a nondissipative skew-symmetric component and a dissipative symmetric component.

2. A splitting technique permitting extension of the dissipative component of the approximation to hyperbolic systems of equations. This includes both upwind schemes with inherent dissipation based on flux-vector or flux-difference splitting and central schemes with explicitly added dissipation.

*Professor, Member AIAA, dwz@oddjob.utias.utoronto.ca
†Graduate Student, stan@oddjob.utias.utoronto.ca
‡Graduate Student, marian@oddjob.utias.utoronto.ca
§Senior Research Scientist, Associate Fellow AIAA, pulliam@nas.nasa.gov

3. A limiting technique which enforces monotonicity or positivity of specific elements of the solution through appropriate use of a first-order discretization in the vicinity of shock waves and other unresolved regions of high gradient.

The strategy chosen for adding numerical dissipation in the discretization of the inviscid fluxes can have a major impact on the accuracy of the overall spatial discretization. Allmaras[1] used grid convergence studies to demonstrate the improvement in accuracy associated with the use of a flux-difference split upwind scheme over the scalar artificial dissipation scheme of Jameson et al.[2] in the computation of laminar boundary layers. Frew at al.[3] also used grid convergence studies to show that the matrix artificial dissipation scheme of Swanson and Turkel[4] is considerably more accurate than the scalar scheme in computing turbulent flows over airfoils. Similarly, Nemec and Zingg[5] showed that the convective upstream split pressure (CUSP[6,7]) scheme of Tatsumi et al.[8] is competitive with matrix dissipation at a reduced cost. A further comparison of the scalar, matrix, and CUSP schemes is presented by Swanson et al.[9]

For applications to the Navier-Stokes equations, it is common to combine a third-order upwind-biased approximation for the inviscid flux terms with a second-order approximation for the viscous fluxes, on the assumption that the error introduced in the differencing of the viscous fluxes is small. The results of De Rango and Zingg[10] suggest that this assumption is questionable in computations of turbulent flows over airfoils. Accurate prediction of drag requires low numerical errors in boundary layers, which are dominated by a balance between the viscous and inviscid fluxes in the streamwise momentum equation. In this region, an error in the viscous flux approximation is just as significant as an error in the inviscid fluxes. De Rango and Zingg showed that with a careful treatment of all relevant approximations, including those used near boundaries as well as the integration technique used to calculate forces and moments, significant reduction in numerical error can be achieved.

The purpose of this paper is to compare the accuracy of four different spatial discretizations for a range of aerodynamic flows. The first uses matrix artificial dissipation, as implemented by Frew at al.,[3] together with second-order centered differences. The second uses the CUSP scheme, as implemented by Nemec and Zingg,[5] again in combination with second-order centered differences. The third discretization is an upwind-biased scheme using flux-difference splitting based on the Roe average,[11] as implemented by Jespersen et al.[12] These discretizations use a second-order approximation for the viscous derivatives. The fourth discretization under study is the algorithm of De Rango and Zingg,[10] which uses fourth-order centered differences with matrix artificial dissipation for the convective terms and fourth-order differencing for the viscous terms. Grid convergence studies are used to determine the numerical error produced by each scheme. Such studies provide a reliable means for assessing numerical error, as demonstrated by Zingg,[13] and are an important component of the code verification process.[14]

Governing Equations and Numerical Methods

The spatial discretizations under study are implemented in ARC2D, developed at the NASA Ames Research Center,[15] which is the basis for the widely used code OVERFLOW.[12] ARC2D uses a generalized curvilinear coordinate system and the diagonal form[16] of the Beam-Warming approximate factorization algorithm with local time stepping. The effects of turbulence are modelled using the Baldwin-Lomax model, and a far-field circulation correction is included at the outer boundary.[15]

Governing Equations

In two-dimensional generalized coordinates, the thin-layer Navier-Stokes equations are given by[15]

$$\frac{\partial \widehat{Q}}{\partial t} + \frac{\partial \widehat{E}}{\partial \xi} + \frac{\partial \widehat{F}}{\partial \eta} = \frac{\partial \widehat{S}}{\partial \eta} \tag{1}$$

where $\widehat{Q} = J^{-1}Q = J^{-1}[\rho, \rho u, \rho v, e]^T$ is the vector of conservative dependent variables, $\widehat{E}$ and $\widehat{F}$ are the convective flux vectors, $\widehat{S}$ is the viscous flux vector, ξ and η are the streamwise and normal generalized coordinates, respectively, and J is the Jacobian of the coordinate transformation.

Applying implicit Euler time-marching to the discretized form of Eq. 1 with a local time linearization, one obtains:

$$[I + h\delta_\xi \hat{A}^n + h\delta_\eta \hat{B}^n - h\delta_\eta \hat{M}^n]\Delta\hat{Q}^n = \hat{R} \tag{2}$$

where

$$\hat{R}^n = -h[\delta_\xi \hat{E}(\hat{Q}^n) + \delta_\eta \hat{F}(\hat{Q}^n) - \delta_\eta \hat{S}(\hat{Q}^n)] \tag{3}$$

The time-step is denoted by h, $\hat{Q}^n = \hat{Q}(nh)$, $\Delta\hat{Q}^n = \hat{Q}^{n+1} - \hat{Q}^n$, and δ denotes a generic spatial operator. The matrices $\hat{A}$, $\hat{B}$, and $\hat{M}$ are the flux Jacobians, defined by

$$\hat{A} = \frac{\partial \hat{E}}{\partial \hat{Q}}, \quad \hat{B} = \frac{\partial \hat{F}}{\partial \hat{Q}}, \quad \hat{M} = \frac{\partial \hat{S}}{\partial \hat{Q}} \tag{4}$$

The diagonalized, approximately-factored form of Eq. 2 is:

$$T_\xi[I + \delta_\xi \Lambda_\xi]\hat{N}[I + \delta_\eta \Lambda_\eta]T_\eta^{-1}\Delta\hat{Q}^n = \hat{R}^n \tag{5}$$

where

$$\hat{N} = T_\xi^{-1}T_\eta \tag{6}$$

The matrices Λ_ξ and Λ_η are diagonal matrices whose elements are the eigenvalues of the flux Jacobians, including a contribution from the viscous flux Jacobian. The matrix T_ξ has the eigenvectors of $\hat{A}$ as columns and T_η has the eigenvectors of $\hat{B}$ as columns.

Matrix Dissipation Scheme

The matrix dissipation scheme[4] is implemented in the following manner:*

$$\frac{\partial \hat{E}}{\partial \xi} \approx \delta_\xi \hat{E} - \nabla_\xi D_1 D_2 \tag{7}$$

with

$$\begin{aligned}
D_1 &= |\widehat{A}|_{j+\frac{1}{2},k} J^{-1}_{j+\frac{1}{2},k} \\
D_2 &= \epsilon^{(2)}_{j+\frac{1}{2},k} \Delta_\xi Q_{j,k} - \epsilon^{(4)}_{j+\frac{1}{2},k} \nabla_\xi \Delta_\xi \nabla_\xi Q_{j,k} \\
\epsilon^{(2)}_{j,k} &= \kappa_2 \max(\Upsilon_{j+1,k}, \Upsilon_{j,k}, \Upsilon_{j-1,k}) \\
\epsilon^{(4)}_{j,k} &= \max(0, \kappa_4 - \epsilon^{(2)}_{j,k}) \\
\Upsilon_{j,k} &= \frac{|p_{j+1,k} - 2p_{j,k} + p_{j-1,k}|}{|p_{j+1,k} + 2p_{j,k} + p_{j-1,k}|}
\end{aligned}$$

where δ_ξ is a centered difference operator, Δ_ξ and ∇_ξ are first-order forward and backward difference operators, κ_2 takes values between 0.5 and 2, and $\kappa_4 = 0.02$. Here we use $\kappa_2 = 0$ for subsonic flows, and $\kappa_2 = 0.5$ for transonic flows. The term $\Upsilon_{j,k}$ is a simple pressure switch to control the use of first-order dissipation near shock waves. The matrix $|\hat{A}|$ is given by

$$|\hat{A}| = T_\xi |\Lambda|_\xi T_\xi^{-1} \tag{8}$$

and

$$|\Lambda|_\xi = \begin{bmatrix} |U| & 0 & 0 & 0 \\ 0 & |U| & 0 & 0 \\ 0 & 0 & |U + c\,\theta| & 0 \\ 0 & 0 & 0 & |U - c\,\theta| \end{bmatrix} \tag{9}$$

where U is the contravariant velocity component in the ξ direction, c is the speed of sound, and $\theta = \sqrt{\xi_x^2 + \xi_y^2}$. In evaluating $|\hat{A}|_{j+\frac{1}{2},k}$ we have used the simple average, although the Roe average is recommended for flows containing very strong shock waves. To avoid zero eigenvalues, the elements of $|\Lambda|_\xi$ are modified as follows:

$$\begin{aligned}
\tilde{\lambda}_1, \tilde{\lambda}_2 &= \max(\lambda_{1,2}, V_l \sigma) \\
\tilde{\lambda}_3 &= \max(\lambda_3, V_n \sigma) \\
\tilde{\lambda}_4 &= \max(\lambda_4, V_n \sigma)
\end{aligned} \tag{10}$$

where σ is the spectral radius of the flux Jacobian. We use $V_l = V_n = 0$ for subsonic flows, and $V_l = 0.025$, $V_n = 0.25$ for transonic flows.

*An analogous term appears in the η direction.

CUSP Scheme

The CUSP scheme[6,7] is formulated by a combination of differences of the state and flux vectors. We consider the ECUSP version only, and refer to it as the CUSP scheme for the remainder of the paper.

For the first-order CUSP scheme, the dissipative flux for the ξ coordinate direction is added as follows:

$$\frac{\partial \hat{E}}{\partial \xi} \approx \delta_\xi \hat{E} - \nabla_\xi d \tag{11}$$

where

$$\begin{aligned}
d_{j+\frac{1}{2},k} &= \frac{1}{2} J^{-1}_{j+\frac{1}{2},k} \alpha^\star_{j+\frac{1}{2},k} c \left(Q_{j+1,k} - Q_{j,k}\right) \\
&\quad + \frac{1}{2} J^{-1}_{j+\frac{1}{2},k} \beta_{j+\frac{1}{2}} \Delta \hat{E}_{j+\frac{1}{2},k}
\end{aligned} \tag{12}$$

with

$$\begin{aligned}
\Delta \hat{E}_{j+\frac{1}{2},k} &= \xi_{x_{j+\frac{1}{2},k}} \left(E_{j+1,k} - E_{j,k}\right) \\
&\quad + \xi_{y_{j+\frac{1}{2},k}} \left(F_{j+1,k} - F_{j,k}\right)
\end{aligned}$$

The vectors E and F are the flux vectors written in Cartesian coordinates. The parameters $\alpha^\star$ and β are given by

$$\alpha^\star c = \alpha c - \beta \overline{U} \tag{13}$$

$$\beta = \begin{cases} \max\left(0, \frac{\overline{U} + \lambda^-}{\overline{U} - \lambda^-}\right) & \text{if } 0 \le M \le 1 \\ -\max\left(0, \frac{\overline{U} + \lambda^+}{\overline{U} - \lambda^+}\right) & \text{if } -1 \le M < 0 \\ \text{sign(M)} & \text{if } |M| > 1 \end{cases} \tag{14}$$

where

$$\lambda^\pm = U \pm c\sqrt{\xi_x^2 + \xi_y^2}$$

and α is chosen to equal $|\overline{U}|/c$. The symbol $\overline{U}$ denotes the arithmetic mean contravariant velocity, while the eigenvalues $\lambda^\pm$ are determined at the Roe state.

To construct a higher-order CUSP scheme, limiters are added which activate near flow discontinuities. We use the following limiter function given by Nemec and Zingg:[5]

$$R(u,v) = 1 - \left| \frac{u - v}{|u| + |v| + \frac{\varepsilon}{|u|+|v|}} \right|^q \tag{15}$$

which is based on Jameson's[6] limiter, with $q = 2$ and $\varepsilon = 10^{-3}$. A higher-order CUSP scheme is obtained by defining the limited average,

$$L(u,v) = \frac{1}{2} R(u,v)\,(u + v) \tag{16}$$

and then constructing the appropriate left and right states for each variable,

$$\begin{aligned}
Q_L^{(m)} &= Q_j^{(m)} + \frac{1}{2} L\left(\Delta Q^{(m)}_{j+\frac{3}{2},k}, \Delta Q^{(m)}_{j-\frac{1}{2},k}\right) \\
Q_R^{(m)} &= Q_{j+1}^{(m)} - \frac{1}{2} L\left(\Delta Q^{(m)}_{j+\frac{3}{2},k}, \Delta Q^{(m)}_{j-\frac{1}{2},k}\right)
\end{aligned} \tag{17}$$

where the superscript m indicates the mth element of the state vector. Consequently, the dissipative flux becomes

$$\begin{aligned} d_{j+\frac{1}{2},k} &= \frac{1}{2} J^{-1}_{j+\frac{1}{2},k} \alpha^{\star}_{j+\frac{1}{2},k} \left(Q_{R,k} - Q_{L,k}\right) \\ &+ \frac{1}{2} J^{-1}_{j+\frac{1}{2},k} \beta_{j+\frac{1}{2}} \Delta E(Q_{R,L_{j+\frac{1}{2},k}}) \end{aligned} \tag{18}$$

where

$$\begin{aligned} \Delta E(Q_{R,L_{j+\frac{1}{2},k}}) &= \xi_{x_{j+\frac{1}{2},k}} \left(E(Q_{R,k}) - E(Q_{L,k})\right) \\ &+ \xi_{y_{j+\frac{1}{2},k}} \left(F(Q_{R,k}) - F(Q_{L,k})\right) \end{aligned}$$

Analogous terms appear in the η direction.

Near domain boundaries, it is necessary to modify the left and right states. At the first interior node the left state becomes

$$Q_L^{(m)} = Q_j^{(m)} + \frac{1}{2} L \left(\Delta Q^{(m)}_{j+\frac{3}{2},k}, \Delta Q^{(m)}_{j+\frac{1}{2},k} \right) \tag{19}$$

while the right state remains unmodified. At the last interior node, the left state does not require modification, but the right state becomes

$$Q_R^{(m)} = Q_{j+1}^{(m)} - \frac{1}{2} L \left(\Delta Q^{(m)}_{j+\frac{1}{2},k}, \Delta Q^{(m)}_{j-\frac{1}{2},k} \right) \tag{20}$$

Application of the limiter to each variable adds considerable computational expense to the algorithm compared to the simple pressure switch. The limiter value has to be computed for each state variable at each node for each direction (i.e., eight evaluations of the limiter function) compared to just two evaluations per node of the pressure switch function. Further, the inversion of the left-hand-side of the implicit algorithm becomes less efficient due to the fact that the limiter may apply different values to each conservation equation. To increase the efficiency of the algorithm we use the same limiter value in each equation, which is based on the pressure. This reduces the computational cost of the limiter to roughly the same level as that of the pressure switch.

Upwind-Biased Scheme

The third-order upwind-biased operator for the inviscid fluxes has the following form when applied to a scalar function:

$$\delta_x q_j = \frac{1}{6\Delta x}(q_{j-2} - 6q_{j-1} + 3q_j + 2q_{j+1}) \tag{21}$$

This can be written as the sum of a fourth-order skew-symmetric component and a third-order symmetric component as follows:

$$\begin{aligned} \delta_x q_j &= \frac{1}{12\Delta x}[(-q_{j+2} + 8q_{j+1} - 8q_{j-1} + q_{j-2}) \\ &+ (q_{j+2} - 4q_{j+1} + 6q_j - 4q_{j-1} + q_{j-2})] \end{aligned} \tag{22}$$

Hence it is equivalent to a fourth-order central scheme with a third-order dissipative component. This is implemented using Roe's flux difference splitting with an entropy fix. A limited extrapolation of the primitive variables is used to calculate the necessary left and right states.

We use the limiter function of Koren[17] with the modification proposed by Venkatakrishnan,[18] which can be written for the ξ direction as follows:

$$\begin{aligned} \tilde{\Psi}_j &= \frac{3\delta^-\delta^+ + (0.1\ \theta)^3}{2(\delta^+ - \delta^-)^2 + 3\delta^-\delta^+ + (0.1\ \theta)^3} \\ \Psi_j &= \min(1, \max(0, \tilde{\Psi}_j)) \end{aligned} \tag{23}$$

where $\delta^- = q_j - q_{j-1}$, $\delta^+ = q_{j+1} - q_j$, and $\theta = \sqrt{\xi_x^2 + \xi_y^2}$. Similar results are obtained using the limiter function of Van Albada et al.[19] The limiters are not used for the subsonic cases.

Higher-Order Algorithm

The higher-order algorithm uses the following operators to approximate first derivatives:[10]

Interior (4th-order)

$$\delta_x q_j = \frac{1}{12\Delta x}(-q_{j+2} + 8q_{j+1} - 8q_{j-1} + q_{j-2}) \tag{24}$$

First Interior Node (3rd-order)

$$\delta_x q_j = \frac{1}{6\Delta x}(-2q_{j-1} - 3q_j + 6q_{j+1} - q_{j+2}) \tag{25}$$

Boundary (3rd-order)

$$\delta_x q_j = \frac{1}{24\Delta x}(-11q_j + 18q_{j+1} - 9q_{j+2} + 2q_{j+3}) \tag{26}$$

The last equation is required only for the calculation of grid metrics. Elsewhere, the grid metrics are evaluated using the same operators as the inviscid fluxes without numerical dissipation.

The standard third-order operator is used for the numerical dissipation:

$$\frac{1}{\Delta x}\left(q_{j+2} - 4q_{j+1} + 6q_j - 4q_{j-1} + q_{j-2}\right) \tag{27}$$

At near-boundary nodes, the following operator is used:

$$\frac{1}{\Delta x}(-q_{j-1} + 3q_j - 3q_{j+1} + q_{j+2}) \tag{28}$$

The viscous terms are in the following general form:

$$\partial_x(\alpha_j \partial_x \beta_j) \tag{29}$$

The following fourth-order expression is used to calculate the $\partial_x \beta_j$ term at half nodes:

$$\begin{aligned} (\delta_x \beta)_{j+\frac{1}{2}} &= \frac{1}{24\Delta x}(\beta_{j-1} - 27\beta_j \\ &+ 27\beta_{j+1} - \beta_{j+2}) \end{aligned} \tag{30}$$

Near boundaries, the following third-order expression is used:

$$(\delta_x\beta)_{j+\frac{1}{2}} = \frac{1}{24\Delta x}(-23\beta_j + 21\beta_{j+1} + 3\beta_{j+2} - \beta_{j+3}) \tag{31}$$

The value of $\alpha_{j+\frac{1}{2}}$ in Eq. 29 is determined using the following fourth-order interpolation formula:

$$\alpha_{j+\frac{1}{2}} = \frac{1}{16}(-\alpha_{j-1} + 9\alpha_j + 9\alpha_{j+1} - \alpha_{j+2}) \tag{32}$$

Near boundaries, a third-order formula is used:

$$\alpha_{j+\frac{1}{2}} = \frac{1}{8}(3\alpha_j + 6\alpha_{j+1} - \alpha_{j+2}) \tag{33}$$

The complete operator is then found from:

$$\begin{aligned}\delta_x(\alpha_j\delta_x\beta_j) = \frac{1}{24\Delta x}(&\alpha_{j-3/2}(\delta_x\beta)_{j-3/2} \\ &-27\alpha_{j-1/2}(\delta_x\beta)_{j-1/2} \\ &+27\alpha_{j+1/2}(\delta_x\beta)_{j+1/2} \\ &-\alpha_{j+3/2}(\delta_x\beta)_{j+3/2})\end{aligned} \tag{34}$$

in the interior, and

$$\begin{aligned}\delta_x(\alpha_j\delta_x\beta_j) = \frac{1}{24\Delta x}(&-23\alpha_{j-1/2}(\delta_x\beta)_{j-1/2} \\ &+21\alpha_{j+1/2}(\delta_x\beta)_{j+1/2} \\ &+3\alpha_{j+3/2}(\delta_x\beta)_{j+3/2} \\ &-\alpha_{j+5/2}(\delta_x\beta)_{j+5/2})\end{aligned} \tag{35}$$

near boundaries.

The implementation of the Baldwin-Lomax turbulence model requires the calculation of the vorticity at half nodes. This is accomplished using the operators given in Eqs. 30 and 31.

The value of $\hat{Q}$ at a far-field boundary node is calculated as follows:

$$\hat{Q}_{bc} = \frac{1}{2}(\hat{Q}_\infty + \hat{Q}_{ext}) - \frac{1}{2}\mathrm{sign}(\hat{A})(\hat{Q}_\infty - \hat{Q}_{ext}) \tag{36}$$

$$\mathrm{sign}(\hat{A}) = T_\kappa \ \mathrm{sign}(\Lambda_\kappa)\ T_\kappa^{-1} \tag{37}$$

where κ is chosen in the direction normal to the boundary, bc indicates the boundary value, ∞ indicates values obtained from free-stream conditions, and ext indicates values extrapolated from the interior nodes of the mesh. The eigenvalues and eigenvectors are calculated from the mean state, $\hat{Q}_{avg} = \frac{1}{2}(\hat{Q}_\infty + \hat{Q}_{ext})$. The following second-order extrapolation operator is used at the far-field boundary:

$$q_j = 3q_{j+1} - 3q_{j+2} + q_{j+3} \tag{38}$$

The pressure at the airfoil surface is determined from a third-order approximation to $\partial p/\partial n = 0$, which gives

$$p_1 = \frac{1}{11}(18p_2 - 9p_3 + 2p_4) \tag{39}$$

For an adiabatic wall, $\partial T/\partial n = 0$, and, when coupled with the assumption of zero pressure gradient and the perfect gas law, this implies $\partial\rho/\partial n = 0$. Hence the density at the airfoil surface is determined from an expression analogous to Eq. 39. Note that the assumption that $\partial p/\partial n = 0$ is not strictly correct. However, for aerodynamic flows at high Reynolds numbers, the error introduced is very small. We have experimented with extrapolation of pressure with no significant change in the solution. Furthermore, the error introduced is non-ordered,[14] and hence does not affect the conclusions from grid convergence studies. The velocity is zero on the body surface.

For grids with a "C" topology, which are used exclusively in this study, the interpolation at the wake-cut (wc) is computed to fourth-order using the data above and below the wake-cut as follows:

$$q_{k_{wc}} = \frac{1}{6}(-q_{k_{wc}+2} + 4q_{k_{wc}+1} + 4q_{k_{wc}-1} - q_{k_{wc}-2}) \tag{40}$$

Test Cases and Grids

We consider the following four test cases:

1. $M_\infty = 0.16$, $\alpha = 6°$, $Re = 2.88 \times 10^6$, laminar-turbulent transition at 0.05 and 0.8 chords on the upper and lower surfaces, respectively, NACA 0012 airfoil.

2. $M_\infty = 0.16$, $\alpha = 12°$, $Re = 2.88 \times 10^6$, laminar-turbulent transition at 0.01 and 0.95 chords on the upper and lower surfaces, respectively, NACA 0012 airfoil.

3. $M_\infty = 0.7$, $\alpha = 3°$, $Re = 9.0 \times 10^6$, laminar-turbulent transition at 0.05 chords on both surfaces, NACA 0012 airfoil.

4. $M_\infty = 0.729$, $\alpha = 2.31°$, $Re = 6.5 \times 10^6$, laminar-turbulent transition at 0.03 chords on both surfaces, RAE 2822 airfoil.

The transonic cases are from Holst.[20] Experimental data for case 4 can be found in Cook et al.[21] The measured coordinates for the RAE 2822 airfoil are used, as in Maksymiuk et al.,[22] rather than the standard coordinates. Experimental data for cases 1 and 2 can be found in Gregory and O'Reilly.[23]

Table 1 is a summary of the grids used. All of the grids have a "C" topology. The distance to the far-field boundary is 12 chords for all grids. While this is clearly a source of error,[13†] it is not a *discretization* error, and hence will not affect our conclusions.[‡] All grids were generated using an elliptic grid generator, such that the largest distance between nodes is

[†] The error incurred varies with the inverse of the distance to the outer boundary.[14]

[‡] For accurate prediction of drag at high lift conditions, a substantially larger distance to the far-field boundary is recommended.[13]

Grid	Dimensions	Points on Airfoil	Off-Wall Spacing ($\times 10^{-6}$)	Leading Edge Clustering ($\times 10^{-3}$)	Trailing Edge Clustering ($\times 10^{-3}$)
A	1057×193	801	0.23	0.1	0.5
B	529×97	401	0.53	0.2	1.0
C	265×49	201	1.2	0.4	2.0
C2	277×49	213	1.2	0.4	2.0

Table 1 Summary of grids.

one chord (near the far-field boundary). Grid B was generated by removing every second node in both coordinate directions from grid A, and grid C was similarly generated from grid B. This technique produces a sequence of grids suitable for a grid convergence study. We also show results for grid C2, which has additional grid nodes clustered near the upper-surface shock wave for cases 3 and 4. Grids C and C2 have a practical density, suitable for use in three dimensions. Grids A and B are primarily for estimation of solution error.

Results and Discussion

The lift, drag, pressure drag, and friction drag coefficients for the four test cases computed on grids A, B, and C are shown in Figs. 1 to 4. They are plotted versus $1/N$, where N is the number of grid nodes. The methods are labelled as follows:

1. **Matrix** - matrix artificial dissipation with second-order centered differences;
2. **CUSP** - CUSP scheme;
3. **Roe** - third-order upwind-biased scheme for the inviscid terms with second-order centered differences for the viscous terms;
4. **Higher-order** - matrix artificial dissipation with fourth-order centered differences for the inviscid and viscous terms.

All four methods produce very similar results on grid A, as expected. Hence the grid A results provide a reasonable reference solution for estimating the numerical error on grid C. A reasonable goal is to achieve a numerical error in lift and drag of less than one percent on grid C. One might argue that this is unnecessarily stringent, given that errors in drag associated with laminar-turbulent transition and turbulence can be significantly greater than one percent. However, we would like the numerical error to be substantially less than the physical model error, thus permitting accurate assessment of physical model error.

With a few exceptions, the errors in the lift coefficient are below one percent on grid C. All of the methods appear to be roughly equally accurate. Closer inspection of the pressure distributions shows that this is not the case, as we shall see later. The errors in the drag coefficients computed on grid C are much larger. In order to get a true picture of solution accuracy, it is important to examine the individual drag components, pressure and friction drag, since the errors in these components are often of opposite sign. For the two subsonic cases, the benefits of the higher-order scheme are immense. The errors in pressure and friction drag produced by the higher-order scheme on grid C are typically not much more than one percent, and they are generally smaller than those produced by the other three schemes on grid B, which has four times as many nodes. The errors in the drag components from the three remaining schemes are much greater than one percent, even on grid B.

The results of the CUSP scheme, the matrix dissipation scheme, and the upwind-biased scheme are quite similar for the subsonic cases, while the upwind-biased scheme produces the largest errors for the transonic cases. Fig. 5 shows the boundary-layer velocity profiles at 85% chord on the upper surface for case 2 computed on grid C. The grid A results, which provide a grid-independent reference solution, show every fourth grid node. The higher-order scheme is superior to the other schemes, illustrating the importance of raising the accuracy of the discretization of the viscous terms. The higher-order results are virtually grid independent, even on grid C.

For the transonic cases, the higher-order discretization produces the smallest pressure drag error on grid C, but it is nevertheless well in excess of one percent. One source of this error is the first-order dissipation introduced near the shock wave. All of the schemes produce lower pressure drag errors when run without any limiting, i.e., without any first-order dissipation, but visible oscillations result, and robustness can be compromised. Another source of error with the matrix dissipation scheme (thus affecting the higher-order algorithm as well) is the requirement of nonzero values of V_l and V_n in Eq. 10 for transonic flows. This leads to some of the overdissipation characteristic of the scalar artificial dissipation scheme.[3]

Adding nodes near the shock, as in grid C2, does not reduce the pressure drag error significantly. Fig. 6 shows details of the pressure coefficient on the upper surface of the airfoil for cases 3 and 4 computed on grid C2. For the grid A solution, every second grid point is plotted. In case 3, the higher-order algorithm produces an improvement in the shock location rela-

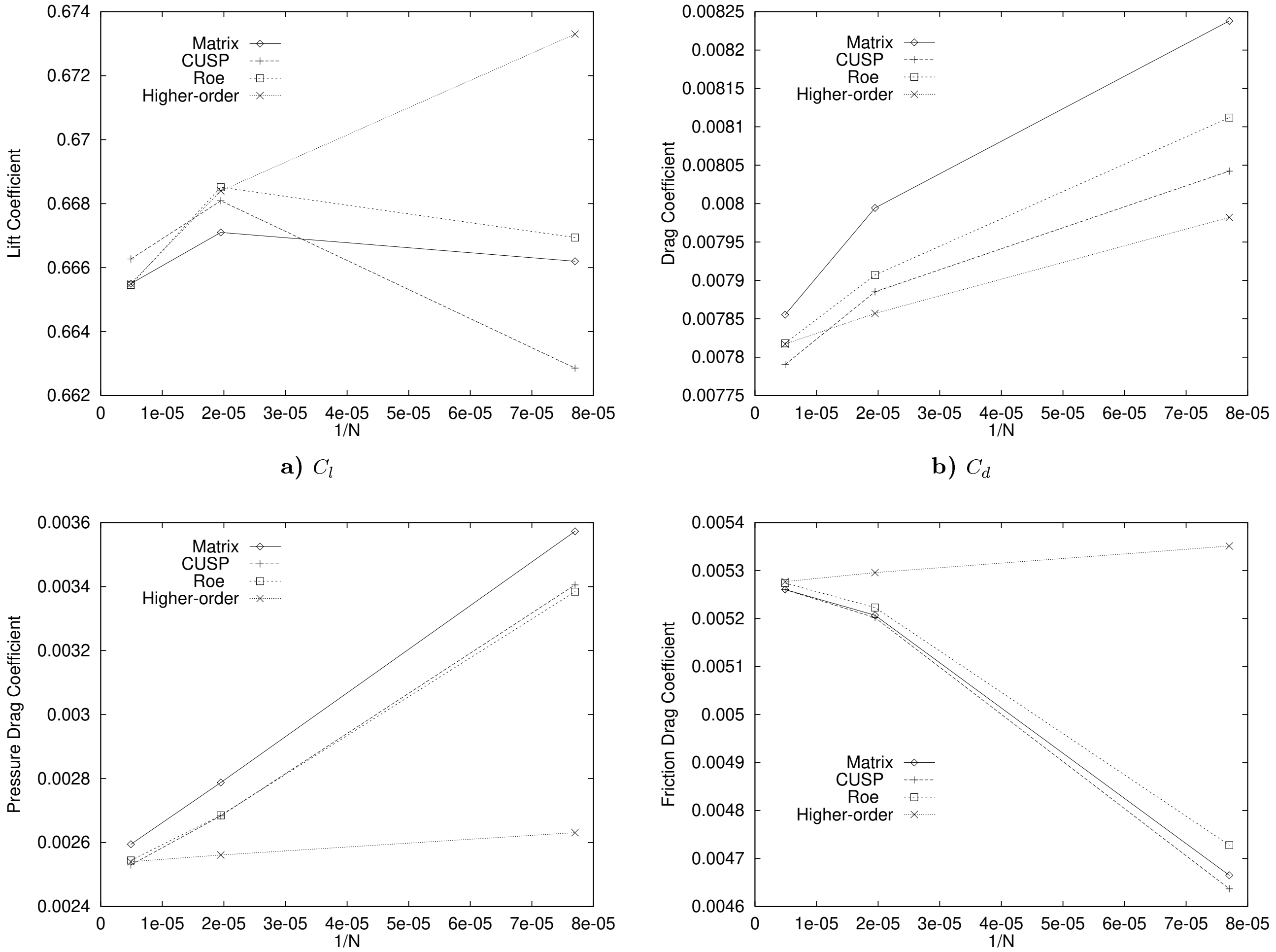

a) C_l **b)** C_d **c)** C_{d_p} **d)** C_{d_f}

Fig. 1 Grid convergence for case 1.

tive to the matrix and CUSP schemes and a significant reduction in error in the low pressure region forward of the shock, with the grid A solution taken as a grid-independent reference. In case 4, the improvement in the shock location is marginal, but the higher-order scheme again produces much smaller errors over the first 20% chord. The grid A results show a spike at the laminar-turbulent transition point which is not seen on the coarser grid C2. The present treatment of transition is grid-dependent and may explain some of the error seen.

In both transonic cases, the upwind-biased scheme produces large errors on grid C2. Since the scheme is competitive with the matrix and CUSP schemes for the subsonic cases, it is clearly the flux limiter which is the source of this error. If the limiter is turned on for the subsonic cases, the drag computed using the upwind-biased scheme increases significantly. This strongly suggests that the limiter is not working properly, since it should have only a minimal effect (preferably none at all) on a subsonic case. We examine this issue further in Fig. 7, which shows the values of the Koren limiter, Eq. 23, and the Nemec-Zingg limiter, Eq. 15, for case 4, grid C. While the Nemec-Zingg limiter is active only near the shock, the Koren limiter is triggered at various locations away from the shock. Hence, in the latter case, excessive first-order error is polluting the solution.

The spatial discretization affects the computational expense on a given grid through its effect on the cost per iteration and on the convergence rate. Of the schemes considered here, the third-order upwind-biased algorithm is the most expensive, followed by the higher-order algorithm, the matrix dissipation scheme with second-order centered differencing, and the CUSP scheme. Applying the limiter to four variables, rather than one, adds significantly to the cost. Other than that, the differences in computational expense are quite small. For example, the higher-order algorithm requires only 5% more processor time than the lower-order scheme with matrix dissipation. Since much coarser grids can be used with the higher-order algorithm while maintaining low numerical error, its overall computational expense needed to achieve a given level of accuracy is by far the least of the schemes considered.

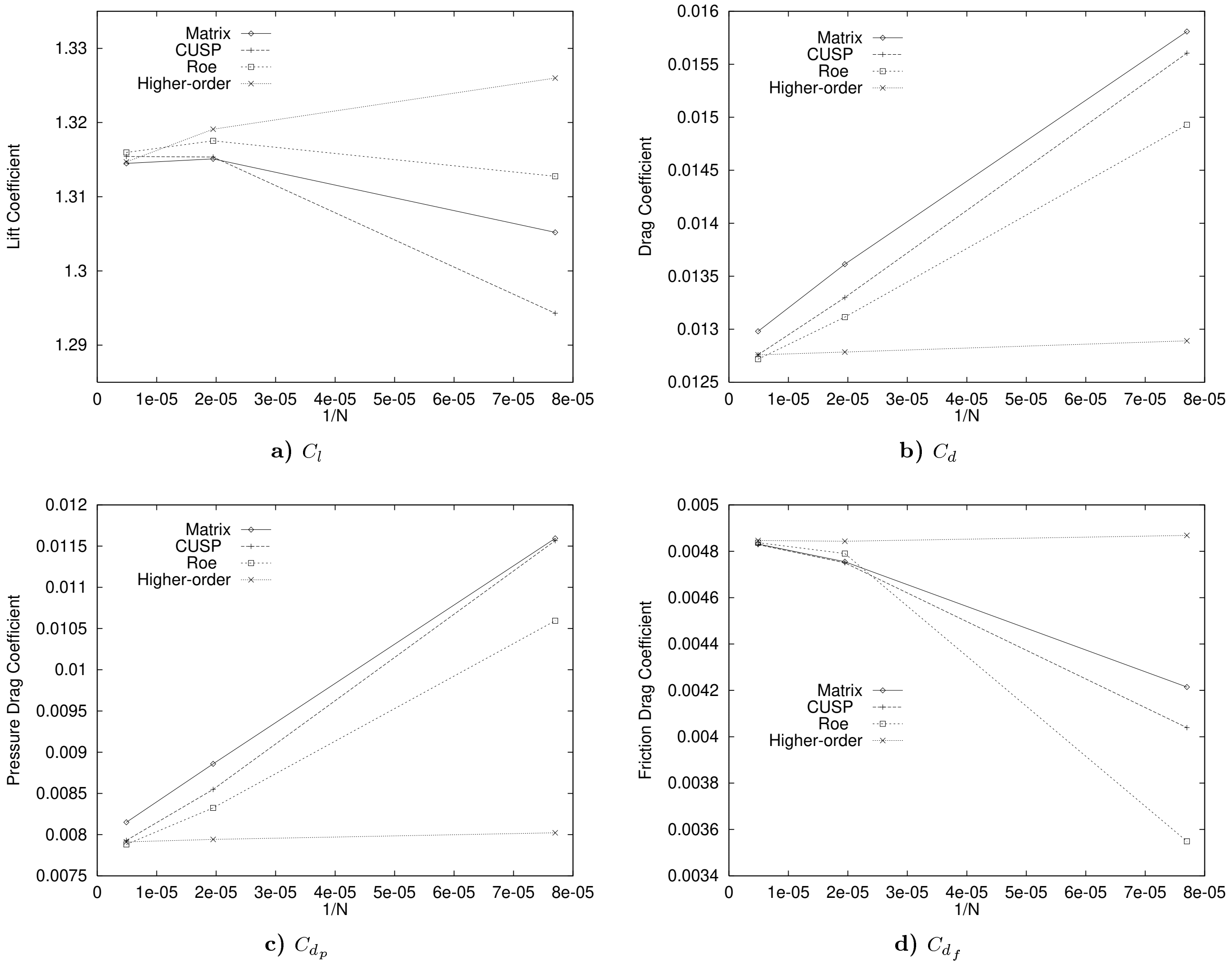

a) C_l **b)** C_d **c)** C_{d_p} **d)** C_{d_f}

Fig. 2 Grid convergence for case 2.

Conclusions

Detailed grid convergence studies have been performed in order to compare the accuracy of several modern spatial discretizations, specifically in the context of subsonic and transonic turbulent flows over airfoils. The following conclusions can be drawn from the results:

1. There is little or no benefit in increasing the order of accuracy of the inviscid flux approximation beyond second order without a corresponding improvement in the accuracy of the viscous flux approximation and other second-order sources of error. This is demonstrated by the fact that the third-order upwind-biased scheme produces no improvement over the second-order schemes, while the scheme with higher-order approximations for both viscous and inviscid terms is more accurate.

2. Matrix dissipation, the CUSP scheme, and flux-difference splitting all lead to comparable accuracy. When coupled with second-order schemes, the numerical dissipation introduced using these approaches is not the largest source of error. This is clearly shown by the accuracy of the higher-order algorithm, which has the same third-order matrix dissipation as the second-order scheme.

3. The popular approach to flux limiting exemplified by the Koren limiter used here can be a major source of error. Most studies of such limiters have emphasized inviscid flows with strong shocks. In the context of transonic turbulent flows over airfoils, our results show that these limiters can do more harm then good, and simpler approaches can be more accurate in addition to being less costly. More research is required to improve these limiter functions to produce good results for this class of flows.

4. Using the higher-order algorithm, less than one percent error in lift and drag can be obtained for subsonic cases on practical grids. A somewhat higher grid density is required for transonic flows. Although the reason is not fully understood, one area which can be improved is the need for the V_n and V_l terms in the matrix dissipation scheme for

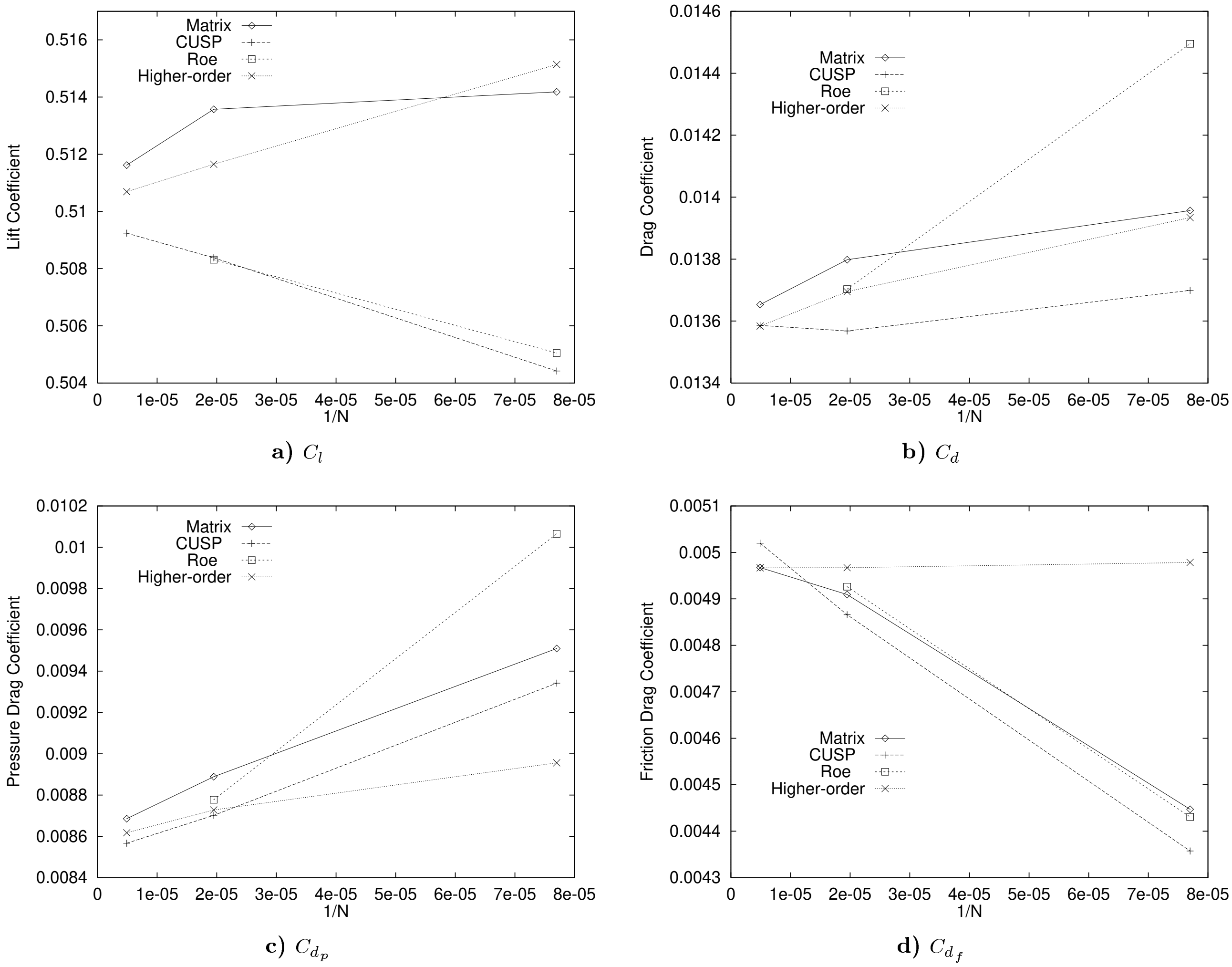

a) C_l **b)** C_d **c)** C_{d_p} **d)** C_{d_f}

Fig. 3 Grid convergence for case 3.

transonic flows.

Once the numerical error is reduced to below one percent on practical grids, one must give serious consideration to other sources of error. These include the thin-layer approximation and the treatment of laminar-turbulent transition. Finally, it would be interesting to see the relative accuracy of algorithms for unstructured grids assessed using grid convergence studies similar to those presented here.

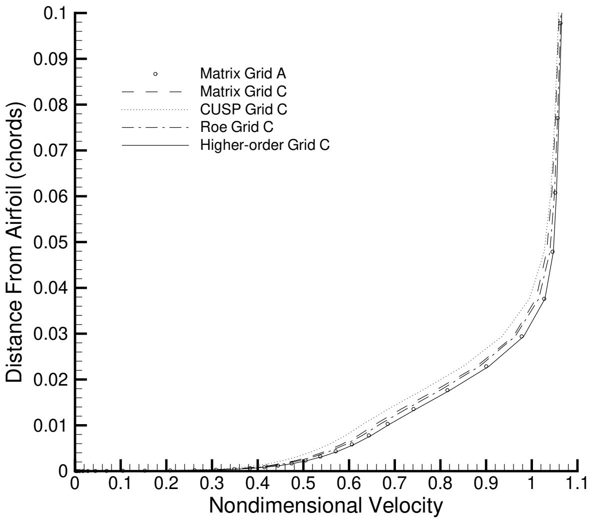

Fig. 5 Boundary layer velocity profiles on the upper surface at 85% chord, case 2.

References

[1]Allmaras, S.R., "Contamination of Laminar Boundary Layers by Artificial Dissipation in Navier-Stokes Solutions," *Numerical Methods for Fluid Dynamics*, edited by M.J. Baines and K.W. Morton, Clarendon, Oxford, UK, 1993.

[2]Jameson, A., Schmidt, W., and Turkel, E., "Numerical Solutions of the Euler Equations by Finite Volume Methods Using Runge-Kutta Time Stepping," AIAA Paper 81-1259, June 1981.

[3]Frew, K., Zingg, D.W., and De Rango, S., "Artificial Dissipation Schemes for Viscous Airfoil Computations," AIAA J., Vol. 36, No. 9, Sept. 1998, pp. 1732-1734.

[4]Swanson, R.C., and Turkel, E., "On Central-Difference and Upwind Schemes," *J. Comp. Phys.*, Vol. 101, 1992, pp. 292-306.

[5]Nemec, M., and Zingg, D.W., "Aerodynamic Computations Using the Convective Upstream Split Pressure Scheme with Local Preconditioning," AIAA Paper 98-2444, June 1998.

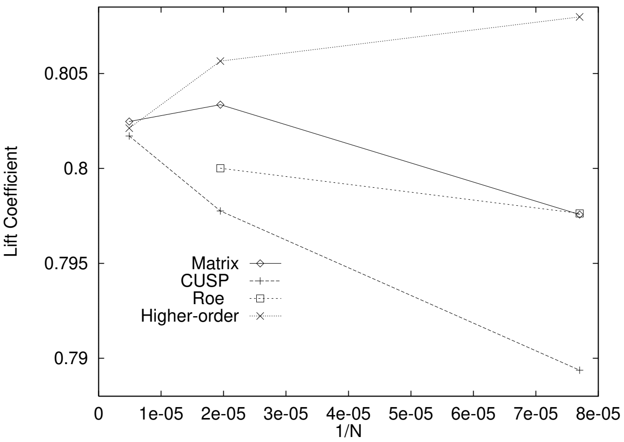

a) C_l

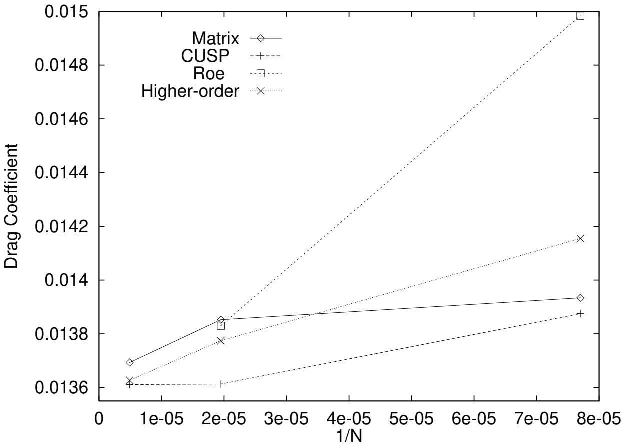

b) C_d

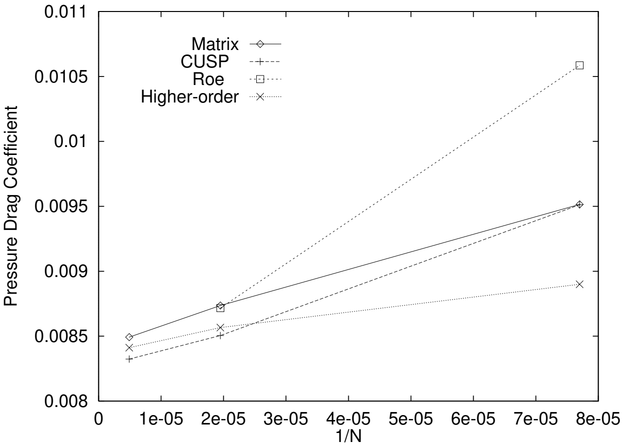

c) C_{d_p}

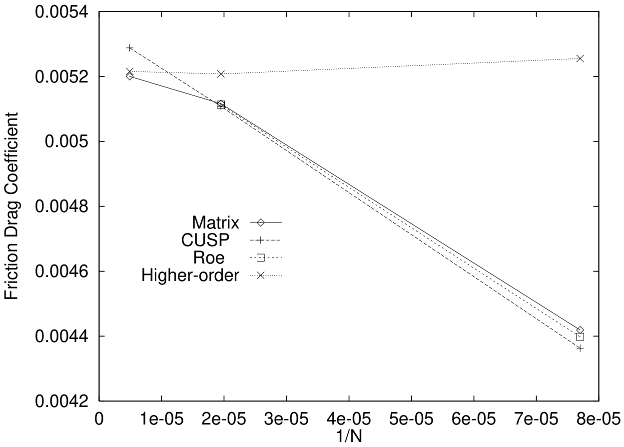

d) C_{d_f}

Fig. 4 Grid convergence for case 4.

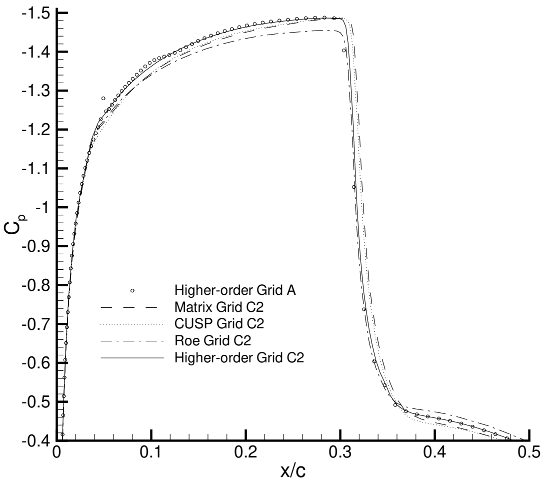

a) Case 3

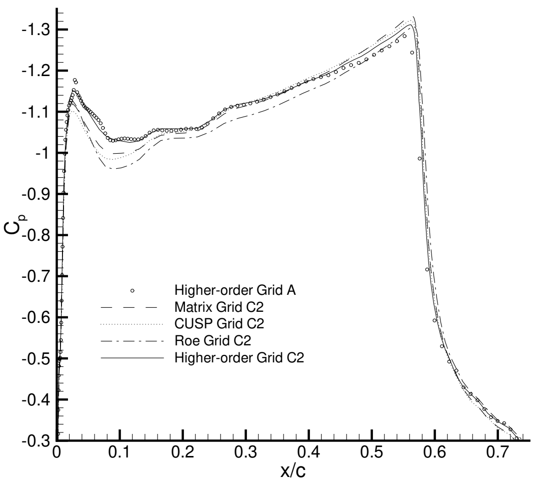

b) Case 4

Fig. 6 Pressure coefficient computed on grid C2.

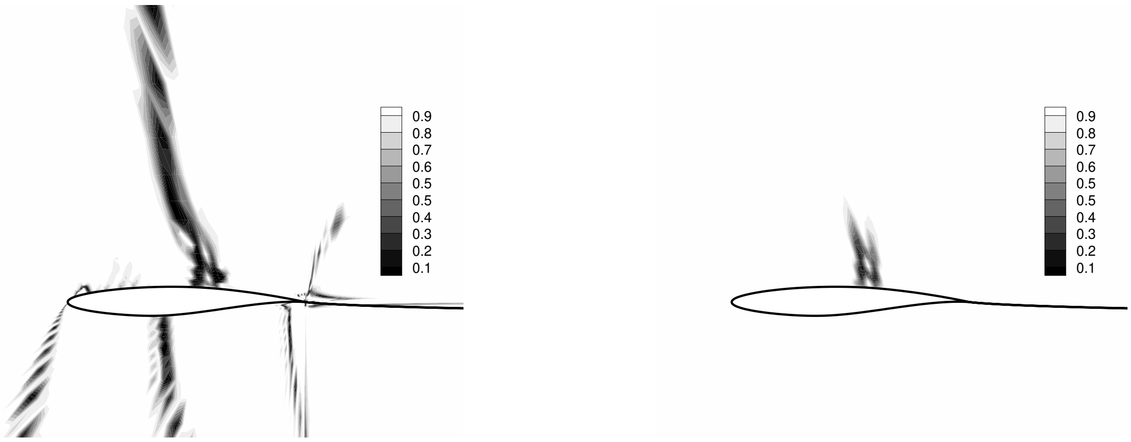

a) Koren limiter **b)** Nemec-Zingg limiter

Fig. 7 Limiter values for case 4.

[6]Jameson, A., "Analysis and Design of Numerical Schemes for Gas Dynamics I: Artificial Diffusion, Upwind Biasing, Limiters and Their Effect on Accuracy and Multigrid Convergence," *Inter. J. Comp. Fluid Dynamics*, Vol. 4, 1995, pp. 171-218.

[7]Jameson, A., "Analysis and Design of Numerical Schemes for Gas Dynamics II: Artificial Diffusion and Discrete Shock Structure," *Inter. J. Comp. Fluid Dynamics*, Vol. 5, 1995, pp. 1-38.

[8]Tatsumi, S., Martinelli, L., and Jameson, A., "A New High Resolution Scheme for Compressible Viscous Flow with Shocks," AIAA Paper 95-0466, Jan. 1995.

[9]Swanson, R.C., Radespiel, R., and Turkel, E., "On Some Numerical Dissipation Schemes," *J. Comp. Phys.*, Vol. 147, 1998, pp. 518-544.

[10]De Rango, S., and Zingg, D.W., "Aerodynamic Computations Using a Higher-Order Algorithm," AIAA Paper 99-0167, Jan. 1999.

[11]Roe, P.L., "Approximate Riemann Solvers, Parameter Vectors, and Difference Schemes," *J. Comp. Phys.*, Vol. 43, 1981, pp. 357-372.

[12]Jespersen, D., Pulliam, T., and Buning, P., "Recent Enhancements to OVERFLOW," AIAA Paper 97-0644, Jan. 1997.

[13]Zingg, D.W., "Grid Studies for Thin-Layer Navier-Stokes Computations of Airfoil Flowfields," *AIAA J.*, Vol. 30, No. 10, 1992, pp. 2561-2564.

[14]Roache, P.J., *Verification and Validation in Computational Science and Engineering*, Hermosa, New Mexico, 1998.

[15]Pulliam, T.H., "Efficient Solution Methods for the Navier-Stokes Equations," Lecture Notes for the Von Karman Institute for Fluid Dynamics Lecture Series, Brussels, Jan. 1986.

[16]Pulliam, T.H., and Chaussee, D.S., "A Diagonal Form of an Implicit Approximate-Factorization Algorithm," *J. Comp. Phys.*, Vol. 39, 1981, pp. 347-363.

[17]Koren, B. "Upwind Schemes, Multigrid and Defect Correction for the Steady Navier-Stokes Equations" Proc. 11th Int. Conf. on Num. Meth. in Fluid Dynamics, edited by D.L. Dwoyer, M.Y. Hussani, and R.G. Voigt, Springer-Verlag, Berlin, 1989.

[18]Venkatakrishnan, V., "Convergence to Steady State Solutions of the Euler Equations on Unstructured Grids with Limiters," *J. Comp. Phys.*, Vol. 118, 1995, pp. 120-130.

[19]Van Albada, G.D., Van Leer, B., and Roberts, W.W., "A Comparative Study of Computational Methods in Cosmic Gas Dynamics," *Astron. Astrophysics*, Vol. 108, 1982, pp. 76-84.

[20]Holst, T.L., "Viscous Transonic Airfoil Workshop Compendium of Results," AIAA Paper 87-1460, June 1987.

[21]Cook, P.H., MacDonald, M.A., and Firmin, M.C.P., "Aerofoil RAE 2822 - Pressure Distributions, and Boundary-Layer and Wake Measurements," AGARD-AR-138, May 1979.

[22]Maksymiuk, C.M., Swanson, R.C., and Pulliam, T.H., "A Comparison of Two Central Difference Schemes for Solving the Navier-Stokes Equations," NASA TM-102815, July 1990.

[23]Gregory, N., and O'Reilly, C.L., "Low-Speed Aerodynamic Characteristics of NACA 0012 Airfoil Section, Including the Effects of Upper-Surface Roughness Simulating Hoar Frost," Aeronautical Research Council, Reports and Memoranda No. 3726, U.K., Jan. 1970.